Ocular Tissue Imaging Using Ultrahigh-Resolution, Full-Field Optical Coherence Tomography

Kate Grieve,[1] *Michel Paques,*[2,3] *Arnaud Dubois,*[1] *José Sahel,*[3] *Claude Boccara,*[1] *and Jean-François Le Gargasson*[3]

Purpose. Ultrahigh-resolution, full-field optical coherence tomography (OCT), which uses a white light source, allows bidimensional, noninvasive tomographic imaging without scanning. The goal of the present study was to apply full-field OCT to ocular tissue imaging in an attempt to explore the capabilities of the technique.

Methods. This full-field OCT system uses a Linnik-type interferometer with a tungsten-halogen source. The spatial resolution is 0.9 × 0.7 μm (transverse × axial). Unstained tissue samples (cornea, lens, retina, choroid, and sclera) and whole, unfixed eyes of rat, mouse, and pig were examined under immersion. A charge-coupled device (CCD) camera recorded a pair of interferometric images that were combined to display en face (i.e., in the *x-y* plane) tomographic images in real time. The acquisition time per tomographic image, which includes summation of 10 raw images, was on the order of 1 s. Postprocessing allows volumetric navigation through the image stack as well as three-dimensional (3D) imaging.

Results. Cellular-level resolution was achieved in isolated tissue samples. En face (*x-y*) images revealed corneal epithelial and stromal cells, lens fibers, nerve fibers, major vessels, and retinal pigment epithelial cells. In *x-z* reconstructions, cellular layers within the cornea and retina and arterioles and venules were clearly defined. Transscleral retinal imaging was achieved in albino animals.

Conclusions. Ultrahigh-resolution, full-field OCT allows cellular-level imaging of unstained ocular tissues with high penetration depth. Although the current system is unsuitable for clinical use, this simple technique has potential for in vivo ocular examination, for which a new system is currently under development. (*Invest Ophthalmol Vis Sci.* 2004;45: 4126–4131) DOI:10.1167/iovs.04-0584

Optical coherence tomography (OCT) is an increasingly popular technique for high-resolution optical imaging, particularly in the field of ophthalmology.[1–4] Its resolution capabilities, penetration depth, and high sensitivity make it suitable for a wide range of biological imaging applications. Both transparent and diffuse tissues can be examined with OCT, although it is in transparent tissue such as the eye that the penetration depth is highest.

To optimize image quality, the choice of light source is critical, as it governs the most important characteristics of OCT: For high tissue penetration, the source must have a wavelength range centered in the near infrared; for high sensitivity, it must have a high irradiance; and for high axial resolution it must have a short coherence length. Because coherence length is inversely proportional to spectrum breadth, a broad-spectrum source is used, meaning that interference occurs only when the optical path length of the two interferometer arms is nearly equal. A precise slice selection in the sample is therefore possible, because the system selects only the signal coming from a slice with a depth proportional to the length of the coherence source. The light is collected by a detector, and that which has interfered (the signal coming from the sample slice of interest) is extracted by modulating the interference fringes. Fringe modulation is most commonly achieved by scanning the reference mirror. The original OCT systems used superluminescent diodes as a light source, providing an axial resolution on the order of 10 μm. This resolution magnitude allows discrimination of retinal layers, but is insufficient for cellular-level imaging. Axial resolution has since been improved to ~1 μm in systems using broadband femtosecond laser technology,[5–7] making cellular-level imaging possible.[8,9] This sophisticated technology, however, remains technically complex and expensive.

In this study, we investigated the advantages of an alternative OCT method that uses a simple thermal light source that presents a broad and smooth spectrum and hence a high axial resolution. The advantages of using full-field (rather than spot) illumination, associated with a silicon charge coupled device (CCD) camera as detector array, include the fact that the need for transverse scanning is avoided, and high-numerical-aperture (NA) microscope objectives may be used to obtain high transverse resolution. Stacks of en face images are recorded to obtain a three-dimensional (3D) data set, from which the construction of multiple two-dimensional (2D) images or 3D volumetric images is possible. Table 1 provides a comparison of conventional OCT performance with that of full-field OCT.

We have previously reported that full-field OCT allows subcellular-level imaging of organisms such as plant leaves and embryos of mouse and frog.[10–13] In this article, the capability of full-field OCT to analyze ocular tissues was evaluated.

Methods

Figure 1 is a schematic representation of our full-field OCT setup. It is based on a bulk Michelson interferometer in the Linnik interference microscope[14] configuration (i.e., with identical water-immersion microscope objectives; 10× −0.3 NA, or 20× −0.5 NA [Olympus, Tokyo, Japan] placed in the arms). Illumination is provided by a 150-W halogen Köhler illuminator (Olympus), which provides an incident illumination on the sample surface of approximately 800 μW. Images

From the [1]Laboratoire d'Optique Physique, Ecole Supérieure de Physique et Chimie Industrielles, Centre National de la Recherche Scientifique, Paris, France; the [2]Ophthalmology Department, Fondation Ophthalmologique Rothschild, Paris, France; and the [3]Laboratoire de Physiopathologie Cellulaire et Moléculaire de la Rétine, Institut National de la Santé et de la Recherche Médicale, Unité 592, Paris, France.

Supported by the Centre National de la Recherche Scientifique and by the European Research Network "Sharp Eye."

Submitted for publication May 25, 2004; revised July 21, 2004; accepted July 25, 2004.

Disclosure: **K. Grieve**, None; **M. Paques**, None; **A. Dubois**, None; **J. Sahel**, None; **C. Boccara**, None; **J.-F. Le Gargasson**, None

The publication costs of this article were defrayed in part by page charge payment. This article must therefore be marked "*advertisement*" in accordance with 18 U.S.C. §1734 solely to indicate this fact.

Corresponding author: Kate Grieve; Laboratoire d'Optique Physique, Ecole Supérieure de Physique et Chimie Industrielles, Centre National de la Recherche Scientifique, UPR A0005, 10 rue Vauquelin, F-75231 Paris Cedex 5, France; grieve@optique.espci.fr.

TABLE 1. Comparison of Conventional OCT and Full-Field OCT

	Conventional OCT	Full-Field OCT
Light source	Superluminescent diode	Tungsten-halogen lamp
Central wavelength	820 nm	770 nm
Bandwidth	25 nm	350 nm
Acquisition device	Photodiode	CCD camera
Spatial resolution	10 × 20 μm (axial × transverse)	0.7 × 0.9 μm (axial × transverse)
Frame size in pixels	On average, 1024 axial × 512 transverse	512 × 512 transverse
Frame acquisition time	1.3 s (400 A-scans/sec)	1 s

are recorded with a silicon CCD camera array (1024 × 1024 pixels, 12 bits, 15 Hz; model 1M15; Dalsa, Waterloo, Ontario, Canada).

The broad-spectrum illumination source has a short coherence length, meaning that interference occurs only when the optical path lengths of the two interferometer arms are almost equal. To extract the interference signal (i.e., the interference of light returning from the reference mirror with that from the sample plane coherent with the mirror), a heterodyne detection scheme is used whereby the camera detection is synchronized with an imposed oscillation of the reference mirror. This oscillation modulates the phase of the interference signal. The camera captures two images in phase opposition during the oscillation period. On calculating the difference of these two images, we extract the interference signal, which corresponds to an en face tomographic image. Several pairs of images can be accumulated to improve the signal-to-noise ratio. The tomographic image is calculated and displayed in real time with a custom Visual C++ program written in-house.

In contrast to confocal microscopy, the parameters that determine the axial and transverse resolutions are independent in OCT. This means that the resolution in the two directions can be optimized individually. Axial resolution is determined by the coherence length of the illumination source, which is inversely proportional to the spectral bandwidth. Our choice of a quartz-tungsten halogen lamp as the source provided us with a broad, smooth spectrum, which, when multiplied by the spectral response of the silicon-based CCD, gave an effective spectrum of width $\Delta\lambda = 350$ nm (full width at half maximum [FWHM]) centered at $\lambda = 770$ nm, and therefore an axial resolution of 0.7 μm in water ($n = 1.33$). Because the average refractive index of the eye is close to that of water, we used identical water-immersion microscope objectives in the sample and reference arms to minimize dispersion mismatch and therefore maintained a high axial resolution through the entire depth of the sample.[14] Because the axial resolution is dependent on the refractive index of the material, the resolution theoretically should change according to the tissue being imaged. This effect is so small, however, that it is visually imperceptible on the images. For example, the center of the lens of refractive index 1.4 decreases the axial resolution to only 0.67 μm, compared with 0.7 μm in water ($n = 1.33$). More important, the axial resolution may be degraded due to dispersion mismatch at increasing depth through the tissue.[15] Quantification of this effect is complicated, but its influence appears to be minimal, because no resolution degradation with depth was apparent on the images. These two resolution-degradation effects are unavoidable in all OCT systems.

Transverse resolution depends on the NA of the optics used in the system. Conventional OCT systems produce cross-sectional (*x-z*) images by scanning the beam in one transverse direction (*x*). In this configuration, a large depth of field is required, equal to the size of the image in the depth direction (*z*), and thus low-NA optics must be used. The resolution in the transverse (*x*) direction is therefore limited. Higher resolution requires the use of zone-focusing and image-fusion techniques.[7] An alternative is to produce en face (*x-y*) OCT images by scanning the beam in two transverse (*x*, *y*) directions.[16,17] In this case, the opportunity exists to use a high NA and thus achieve high transverse resolution. However, the bidirectional scanning generally increases the complexity of the system and the acquisition time, although high-frame-rate, en face OCT has been demonstrated.[18,19] The full-field OCT system produces tomographic images in the en face orientation without scanning. High-NA microscope objectives can be used. The water-immersion objectives used for the acquisition of the images obtained in the study and presented herein have an NA of either 0.3 (10×) or 0.5 (20×), which give a theoretical transverse resolution of 1.4 and 0.8 μm, respectively (the mean wavelength being $\lambda = 800$ nm). In practice, the transverse resolution was measured to be ~1.6 and ~0.9 μm, respectively. Similar to axial resolution, transverse resolution is dependent on refractive index and so has a dependence on tissue and also may be degraded due to dispersion mismatch. However, these effects are so slight that no transverse resolution degradation is apparent on the images. The objectives used have a working distance of 3.3 mm.

High detection sensitivity is reached in OCT due to the interferometric nature of the signal recorded. The amplitude of the light backscattered by the sample is measured rather than the intensity. Various system parameters such as reference mirror reflectivity, incoherent light in the system, and the CCD camera charge capacity influence sensitivity and must be optimized. The sensitivity of our system was measured to be of the magnitude of 80 dB[11]—lower than that offered by laser-based systems[7] but nonetheless ample for our experiments.

Our system produces tomographic images in the *x-y* (en face) orientation. The sample is moved step by step (with a typical step size of 1 μm) in the axial direction to acquire a stack of tomographic images, forming a 3D data set. From this data set, sections in any orientation can be extracted using custom-written software (MatLab; The MathWorks, Natick, MA). Several sections can be projected, to produce an image with extended depth of field, and videos can be made from a succession of sections in any direction.

The various steps of image processing are as follows: First, the dynamic range of the signal is compressed in a logarithmic scale because the OCT signal intensity varies greatly from one image pixel to another. The images presented are therefore logarithmic in scale. It must be noted that this compression degrades the apparent spatial resolution of the images. It is however indispensable in the production of images with sufficient contrast. Images are displayed in gray scale (coded with 256 gray levels) rather than false color, as false colors may produce artifacts in the images and lead to incorrect interpretation of physical structures. In gray scale, white corresponds to the highest signal and black to the lowest. A threshold is applied to subtract the noise background, and the gray-scale histogram is then redistributed in image analysis software (Photoshop; Adobe Systems, Mountain View, CA) to take advantage of all 256 gray levels. Finally, slight Gaussian smoothing of width 0.5 pixels is applied in the software to reduce the noise in our OCT images while maintaining as far as possible the image resolution. This is necessary, as OCT images contain speckle due to the interference of light backscattered by different tissue microstructures located inside the coherence volume.

All animal manipulation was in accordance with the ARVO Statement for the Use of Animals in Ophthalmic and Vision Research. Pigmented and albino rats were deeply anesthetized by pentobarbital and killed by head dislocation. The porcine eyes were obtained from a local abattoir. Eyes were preserved in phosphate-buffered saline (PBS, pH 7) or paraformaldehyde during transfer to the laboratory, dissected with small scissors and forceps, and put in a container filled with PBS. The container was placed on a high-precision motorized linear stage

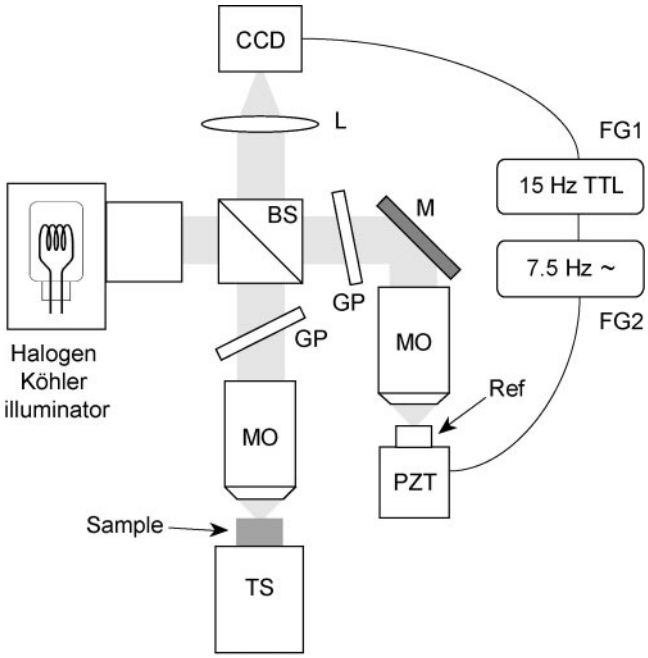

FIGURE 1. Schematic representation of the full-field OCT. The light source is a tungsten halogen lamp in a Köhler illuminator setup. BS, beam splitter; MO, vertically positioned microscope objectives (water-immersion, 10×, 0.3 NA, or 20×, 0.5 NA); M, mirror (silver) for upright reference arm; GP, glass plates for dispersion compensation (antireflection coated); L, aplanatic doublet achromat lens (300-mm focal length); Ref, reference mirror (2% reflectivity); PZT, piezoelectric stage actuator; TS, translation stage; FG1 and FG2, function generators.

that typically moved a distance of 1 μm between consecutive images. A stack of tomographic images were acquired at successive depths, typically in 1-μm steps. The acquisition time for each tomographic image was approximately 1 second (5–10 images accumulated). Post-acquisition volumetric reconstruction then allowed navigation within the image stack in any direction, to allow examination of a given area of interest.

RESULTS

Figure 2a demonstrates transcorneal lens imaging in an albino mouse eye, recorded on a whole eye. Figures 2b–f show images recorded on the isolated lens and cornea extracted from rat eye. In the cornea (Figs. 2a, 2d–f), the contours of epithelial cells, details of the stroma suggestive of keratocytes, and Bowman's and Descemet's membranes are clearly distinguished. In the lens (Figs. 2a, 2b, 2c), the capsule, the epithelial cell layer, and the cortical fibers can be discerned. The interfaces between cells and liquid and/or with membranes appear highly reflective, such as at the level of Descemet's membrane or between the lens capsule and the lens epithelial cells.

Images of the retina are shown in Figure 3. To achieve the image in Figure 3a, we removed the anterior segment from the whole eye and lowered the microscope objective directly into the vitreous. All other images were obtained from isolated retinas. In the rat retina, the nerve fiber bundles (Figs. 3d, 3e) and, within the porcine retina, individual outer segments (Figs. 3f, 3g) are visible. The size of the outer segments suggests that these are cones. Conversely, in the rod-dominant retina of rats, no separation between outer segments of photoreceptors was visible. This was thought to be because the diameter of rods in rats is comparable to or smaller than our resolution capability. In reconstructed *x-z* retinal images of the rat retina (Figs. 3a,

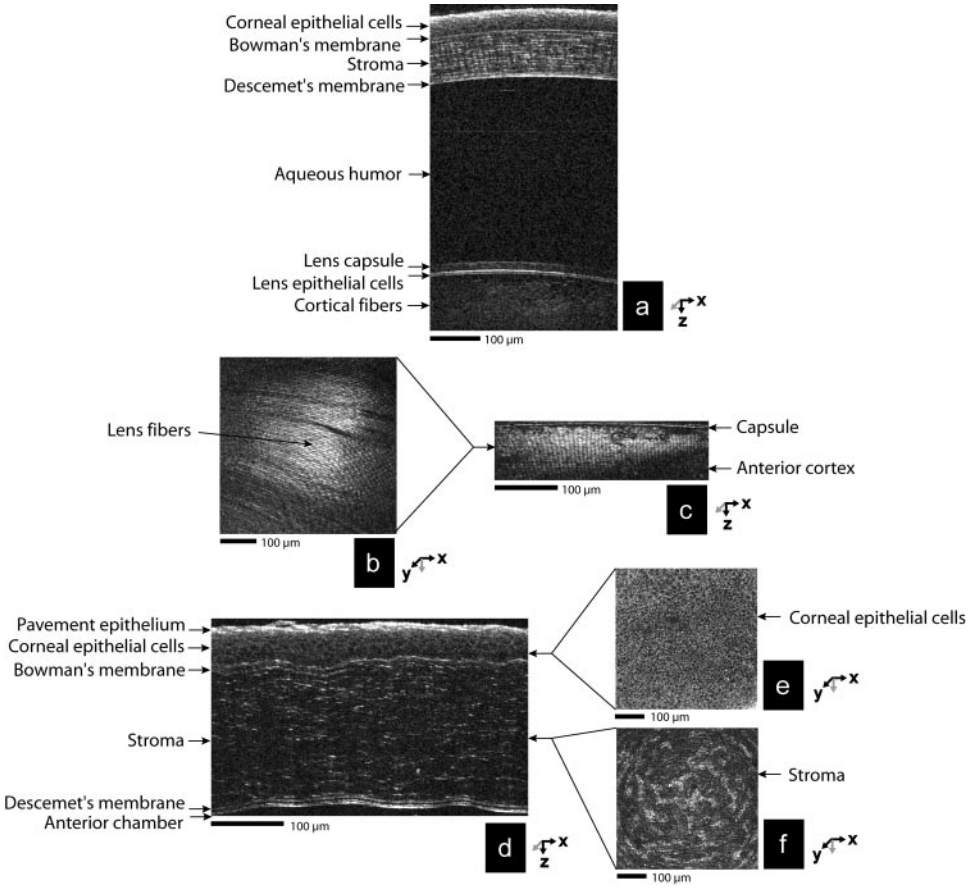

FIGURE 2. Ex vivo full-field OCT imaging of the anterior segment of a whole mouse eye (**a**) and of isolated tissues of a rat eye (**b–f**). The imaging plane (i.e., *x-z* section or *x-y* en face image) is indicated by the *black arrows* in the axes symbol. (**a**) *x-z* reconstruction from a stack of *x-y* (en face) images through the anterior segment showing the cornea, vitreous, and anterior lens cortex of a mouse. (**b**) Raw *x-y* image inside the anterior cortex, the depth location of which is indicated by the *arrow* in (**c**). (**c**) *x-z* reconstruction of the lens anterior cortex. Note the high reflectivity of the lens capsule, the visibility of the lens epithelial cell layer between the two anterior hyperreflective lines, and the underlying lens fibers. The regular array and the curved shape of the lens fibers are clearly revealed. (**d**) *x-z* reconstruction of the cornea. The irregular membrane contours are due to damage to the sample that occurred during transport to the laboratory. *Arrows*: locations of *x-y* images (**e**) and (**f**), respectively. (**e**) Tightly packed epithelial cells; (**f**) keratocytes and stromal fibers. Bar, 100 μm.

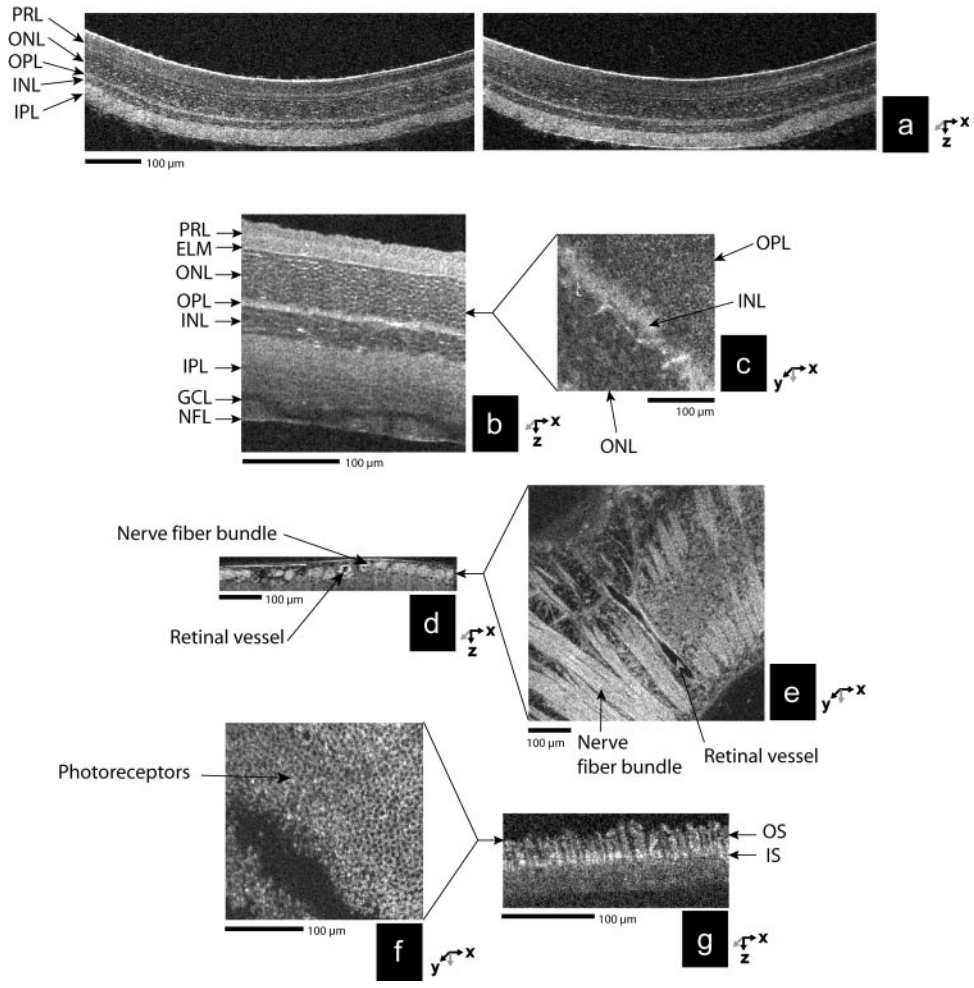

FIGURE 3. Ex vivo full-field OCT imaging of rodent and porcine retina samples. (**a**, **b**) *x-z* reconstructions from stacks of *x-y* images in the rat retina. (**a**, *left*) Image was recorded 2 hours earlier than the other image (*right*). The images were highly reproducible. (**c**) *x-y* image showing the plexiform and nuclear layers. (**d**, **e**) *x-z* and *x-y* images, respectively, of the nerve fiber bundles in the rat retina. (**f**, **g**) *x-y* and *x-z* images, respectively, of pig photoreceptors. Arrows on *x-z* images indicate the depths of the corresponding *x-y* images. PRL, photoreceptor layer; ELM, external limiting membrane; ONL, outer nuclear layer; OPL, outer plexiform layer; INL, inner nuclear layer; IPL, inner plexiform layer; GCL, ganglion cell layer; NFL, nerve fiber layer; OS, outer segment; IS, inner segment. Bar, 100 μm.

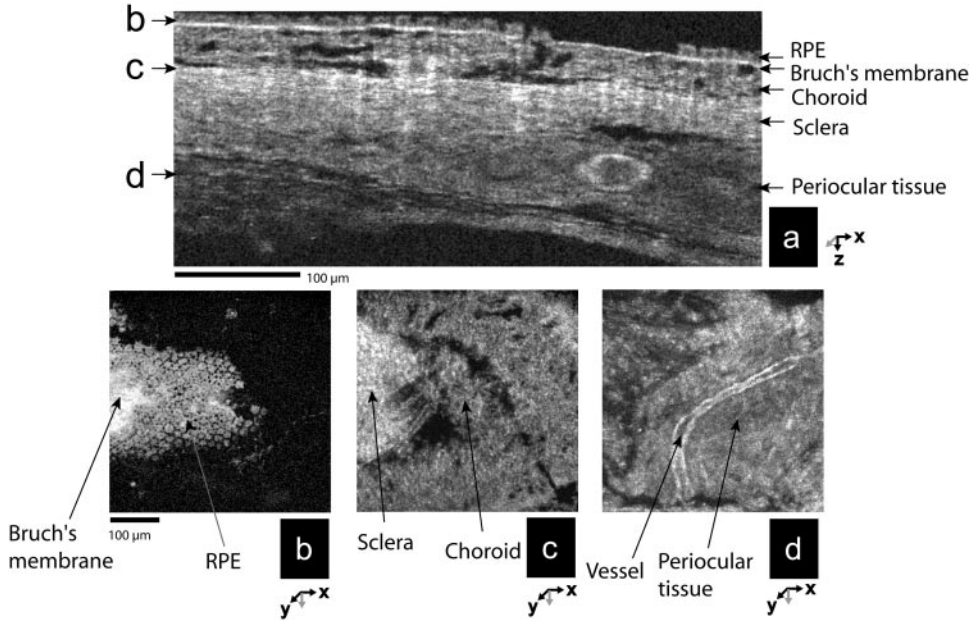

FIGURE 4. Ex vivo full-field OCT imaging through the choroid and sclera of a rat. (**a**) *x-z* reconstruction; (**b–d**) *x-y* images. *Arrows*: the respective depths of images (**b–d**). Note the visibility of the RPE pavement and of Bruch's membrane in (**b**), the limit between the choroid and sclera (**c**), and the transscleral viewing of periocular tissue inside which a vessel is seen (**d**). Bar, 100 μm.

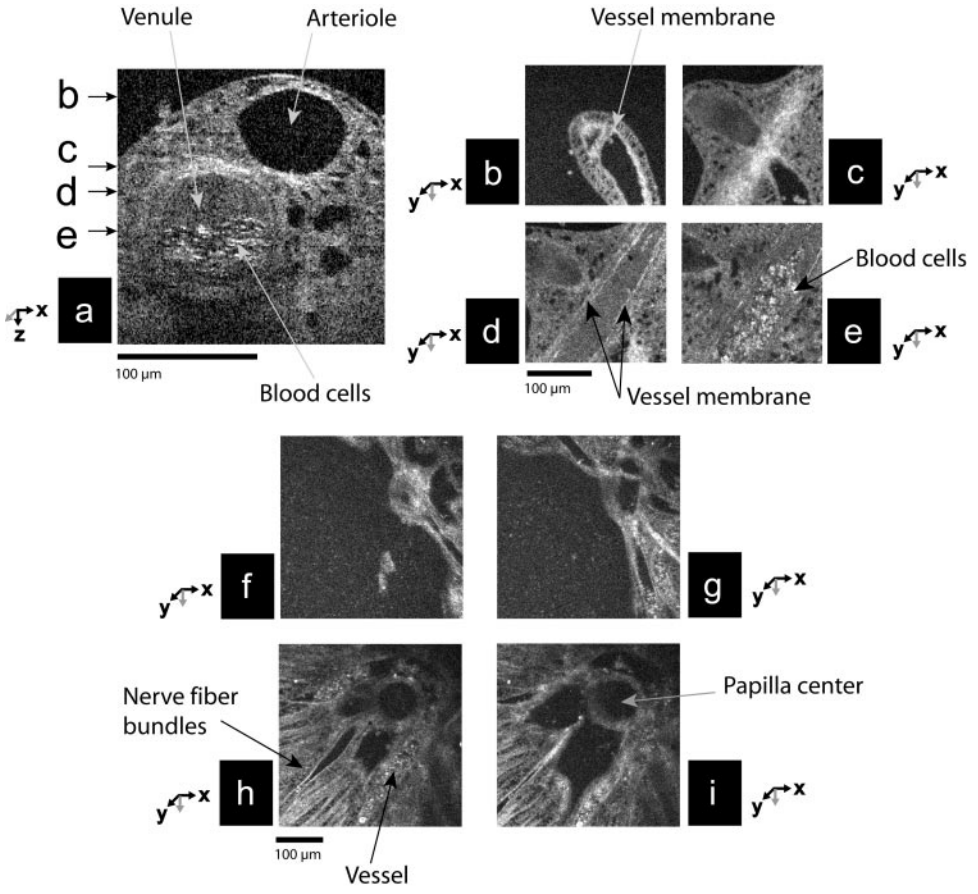

FIGURE 5. Full-field OCT images of an arteriovenous crossing in the porcine retina (**a–e**) and of the disc in the rodent retina (**f–i**). (**a**) *x-z* reconstruction; (**b–e**) *x-y* images. *Arrows* in the *x-z* image indicate the respective depths of the *x-y* images. Successive *x-y* images through the arteriovenous crossing reveal the relationship between the artery on top, and the vein below. The vein is filled with erythrocytes, while the artery is empty. (**f–i**) *x-y* images of the disc in a rat retina. Note the convergence of axons toward the disc and the presence of radiating vessels. The disc appears devoid of reflective structures in the deeper scans, probably because of the perpendicular disposition of the fibers and/or a masking effect of overlying structures. Bar, 100 μm.

3b), the nerve fiber layer, the three nuclear layers, and the plexiform layers are clearly recognizable. The two images in Figure 3a demonstrate reproducibility of images, in this case over a 2-hour period.

In the choroid and sclera, the typical polygonal retinal pigment epithelial pavement, Bruch's membrane, and the random disposition of scleral collagen fibers are observable (Fig. 4).

The penetration of full-field OCT was sufficient to image an arteriovenous crossing (Figs. 5a–e). In the optic nerve, the convergence of axons and vessels are visible (Figs. 5f–i).

To appreciate penetration depth in ocular tissues, we used full-field OCT to examine whole eyes. In the albino mouse eye, transcorneal imaging of the lens (Fig. 2) and transscleral imaging of the retina (Fig. 6) were obtainable. In pigmented mouse eyes, transscleral images of the choroid were obtained, including Bruch's membrane, but the signal returning from the retina was significantly attenuated compared to that in the albino mouse.

DISCUSSION

We show herein the first results of full-field OCT imaging of ocular tissues. These results are of considerable interest because they demonstrate the strength of this technique in imaging unstained ocular tissues with high resolution and penetration depth. The 3D data set offers the possibility of combining en face and cross-sectional images to provide complementary information. Indeed, the en face image can reveal structures that pass unseen in the cross section and vice versa. For instance, the nerve fiber layer is most visible in en face images, while determination of the thickness of retinal or corneal layers appears best performed on cross-sectional im-

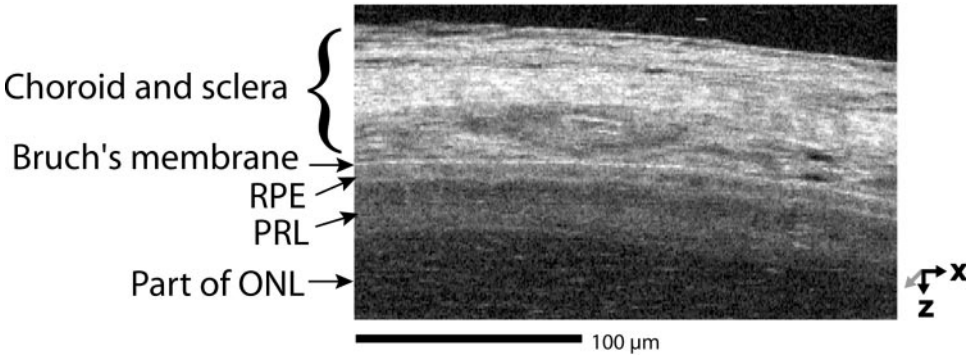

FIGURE 6. Transscleral imaging of the retina in an albino mouse. To appreciate the penetration depth of the full-field OCT technique, a stack of images was acquired by *z* scanning from the outside to the inside of the eye of an albino mouse. Note that retinal structures remained visible. Bar, 100 μm.

ages. Volumetric reconstruction allows further exploitation of the available information through the analysis of a given area of interest from multiple angles.

Preliminary analysis of signal levels arising from different tissues shows that overall, fibrillar structures give a high signal, most strikingly in the lens and also within the nerve fiber layer. Note also that the membranes, such as Bruch's membrane, and also the interface between cells and extracellular milieu, such as the interface between endothelial cells and the anterior chamber, give high signal levels. Complementary in vivo and in vitro studies are needed for better quantification of the interference signal. The high penetration capability of full-field OCT was suggested by the possibility of imaging the choroid and retina through the sclera, at least in albino animals.

The use of the full-field OCT system allows high-resolution imaging of various ocular tissues. Results are highly reproducible. A set of repeated experiments on the same tissue over a prolonged time produces a set of identical images. For example, Figure 3a shows two images of a rat retina recorded 2 hours apart, and no changes are apparent. The imaging process is invariable from one experiment to the next, provided the initial regulation procedures of the instrument are correctly followed by the operator. In certain cases it was noted, however, that slight differences in penetration ability and reflectivity properties of the tissue occurred over a long time (several hours of tissue illumination). These changes appear to be attributable to changes in the nature of the tissue itself. We conclude that should any change in the captured image occur during a set of experiments, it is due to changes in tissue properties (and probable damage to the tissue) and not to experimental setup.

The current setup was specifically designed for ex vivo microscopy purposes, and is therefore unsuitable for clinical applications. However, the relative technical simplicity of the technique holds promise for adaptation to in vivo conditions. Indeed, it is robust (i.e., it uses a sturdy white-light source and requires only *z* scanning, as opposed to the *x-yz* scanning necessary in other OCT systems), and the light source is inexpensive. The current system requires a relatively lengthy image-acquisition time to obtain a satisfactory signal-to-noise ratio. For this technique to be applicable to in vivo examination, exposure time must be considerably reduced, both to comply with safety standards and to eliminate the effect that sample movement would have on the image. Motion in the sample during the acquisition time would induce important changes in the optical phase, making the interference signal blur and the image contrast vanish. The present full-field OCT technique is therefore suitable exclusively in applications in which the sample is immobile (<1 μm displacement) on the time scale of the image acquisition ($\sim$1 s per en face image). In conventional scanning OCT systems, the sample must remain stationary only during the acquisition time per pixel, which is considerably shorter than our acquisition time per image, since we record the image in parallel on every pixel of the CCD. The development of a short-acquisition-time, full-field OCT system is currently under way. Images will be acquired by this system more rapidly than the typical human eye motion, thus avoiding the need for eye fixation. An alternative acquisition device will provide the increase in acquisition speed necessary to freeze the eye motion during image acquisition. A further consideration when imaging the in vivo eye will be dispersion compensation: as it will no longer be feasible to work under immersion to minimize the dispersion effects, the addition of an optical dispersion compensation system is needed, to minimize dispersion before image acquisition.

A possible extension of the current ex vivo study would be to image ex vivo human eyes obtained from an eye bank to gain some indication of what would happen in vivo.

Acknowledgments

The authors thank Valérie Reita and Patrick Piard for mechanical conception and realization and Francis Cassagne and Fabien Lejeune for electronics and computing help.

References

1. Huang D, Swanson EA, Lin CP, et al. Optical coherence tomography. *Science*. 1991;254:1178–1180.
2. Fercher AF. Optical coherence tomography. *J Biomed Opt*. 1996; 1:157–163.
3. Hee MR, Puliafito CA, Wong C, et al. Quantitative assessment of macular edema with optical coherence tomography. *Arch Ophthalmol*. 1995;113:1019–1029.
4. Massin P, Vicaut E, Haouchine B, et al. Reproducibility of retinal mapping using optical coherence tomography. *Arch Ophthalmol*. 2001;119:1135–1142.
5. Bouma B, Tearney GJ, Boppart SA, Hee MR, Brezinski ME, Fujimoto JG. High-resolution optical coherence tomography imaging using a mode-locked Ti:Al_2O_3 laser source. *Opt Lett.* 1995;20:1486–1488.
6. Bouma B, Tearney GJ, Bilinsky IP, Golubovic B, Fujimoto JG. Self phase-modulated Kerr-lens mode locked Cr:forsterite laser source for optical coherence tomography. *Opt Lett*. 1996;21:1839–1841.
7. Drexler W, Morgner U, Kärtner FX, et al. *In vivo* ultrahigh-resolution optical coherence tomography. *Opt Lett*. 1999;24:1221.
8. Boppart SA, Bouma B, Pitris C, Southern JF, Brezinski ME, Fujimoto JG. *In vivo* optical coherence tomography cellular imaging. *Nat Med*. 1998;4:861.
9. Považay B, Bizheva K, Unterhuber A, et al. Submicrometer axial resolution optical coherence tomography. *Opt Lett*. 2002;20: 1800–1802.
10. Vabre L, Dubois A, Boccara AC. Thermal-light full-field optical coherence tomography. *Opt Lett*. 2002;27:530–532.
11. Dubois A, Grieve K, Moneron G, Lecaque R, Vabre L, Boccara AC. Ultrahigh-resolution full-field optical coherence tomography. *Appl Opt*. 2004;43:2874–2883.
12. Dubois A, Moneron G, Grieve K, Boccara AC. Three-dimensional cellular-level imaging using full-field optical coherence tomography. *Phys Med Biol*. 2004;49:1227–1234.
13. Perea-Gomez A, Camus A, Moreau A, et al. Initiation of gastrulation in the mouse embryo is preceded by an apparent shift in the orientation of the anterior-posterior axis. *Curr Biol.* 2004;14:3: 197–207.
14. Dubois A, Vabre L, Boccara AC, Beaurepaire E. High-resolution full-field optical coherence tomography with a Linnik microscope. *Appl Opt*. 2002;41:805–812.
15. Hitzenberger CK, Baumgartner A, Drexler W, Fercher AF. Dispersion effects in partial coherence interferometry: implications for intraocular ranging. *J Biomed Opt*. 1999;4:144–151.
16. Izatt JA, Hee MR, Owen GM, Swanson EA, Fujimoto JG. Optical coherence microscopy in scattering media. *Opt Lett*. 1994;19:590–592.
17. Podoleanu AG, Dobre GM, Jackson DA. *En face* coherence imaging using galvanometer scanner modulation. *Opt Lett*. 1998;23: 147–149.
18. Podoleanu AG, Rogers JA, Jackson DA, Dunne S. Three dimensional OCT images from retina and skin. *Opt Expr*. 2000;7:292–298.
19. Hitzenberger CK, Trost P, Lo P-W, Zhou Q. Three-dimensional imaging of the human retina by high-speed optical coherence tomography. *Opt Expr*. 2003;11:2753–2761.